Journal of *Marine Science and Engineering*

MDPI

Article

A Synthetic Data-Driven Approach for Oil Spill Detection: Fine-Tuning YOLOv11-Seg with LIC-Based Ocean Flow Modeling

Farkhod Akhmedov [1], Khujakulov Toshtemir Abdikhafizovich [2], Furkat Bolikulov [1] and Fazliddin Makhmudov [1,*]

[1] Department of Computer Engineering, Gachon University, Seongnam 13120, Republic of Korea; bolikulovfurkat@mail.ru (F.B.)
[2] Department of Computer Engineering, University of Tashkent for Applied Sciences, Tashkent 100125, Uzbekistan
* Correspondence: fazliddin12@gachon.ac.kr

Abstract

Oil spills represent a severe environmental hazard, threatening marine and coastal ecosystems, biodiversity, and socio-economic stability. Timely and accurate detection of such incidents is critical for mitigating their ecological and economic consequences. Conventional detection techniques, including manual inspection and satellite-based observation, remain limited by high operational costs, temporal delays, and restricted spatial coverage. To overcome these limitations, this study introduces a comprehensive computer vision framework that addresses two core challenges: (i) the construction of a large-scale, high-quality synthetic oil spill dataset through mask extraction and seamless blending of oil spill regions with diverse oceanic backgrounds, and (ii) the development of a fine-tuned YOLOv11m-seg detection model trained on this enriched dataset. To further enhance the realism and spatial distinctiveness of oil spill textures, the Line Integral Convolution (LIC) is applied to estimate and visualize ocean surface flow patterns, generating coherent streamline textures that simulate the natural diffusion and transport of oil in water. The model exhibited strong generalization and precision, achieving a training accuracy exceeding IoU@0.50-0.95 to 85% over 50 epochs. Evaluation metrics confirmed its reliability, with an F1 score of 94%, precision of 94%, and recall (mAP@0.50) of 94%. These results demonstrate that the developed approach not only enhances dataset diversity but also substantially improves the accuracy and representativeness of real-time oil spill detection in marine environments.

Keywords: computer vision; custom dataset generation; oil spill detection; synthetic image blending; ocean wave modeling; marine monitoring

Check for updates

Academic Editors: Marcos Dos Santos and Miguel Ângelo Lellis Moreira

Received: 23 February 2026
Revised: 22 March 2026
Accepted: 23 March 2026
Published: 26 March 2026

Copyright: © 2026 by the authors. Licensee MDPI, Basel, Switzerland. This article is an open access article distributed under the terms and conditions of the Creative Commons Attribution (CC BY) license.

1. Introduction

Detecting oil spills is a critical environmental and socio-economic challenge due to their devastating consequences on marine ecosystems, human livelihoods, and local economies. Oil spills release toxic substances that disturb aquatic ecosystems, threaten biodiversity, and compromise the health of marine and coastal environments. These pollutants infiltrate food chains, cause suffocation in marine species, and lead to long-lasting ecological damage. Beyond environmental repercussions, oil spills also impose severe economic burdens, particularly on communities reliant on fishing and coastal industries. Recovery efforts

are often time-intensive and financially draining, with ecological restoration potentially taking decades to achieve. Overall, oil spills have been a worldwide issue with severe environmental impacts over the years [1].

The urgency of addressing this issue is underscored by the approximately 2000 tons of oil spilled globally in 2023. Historical incidents illustrate the far-reaching consequences of oil spills. For example, the Nowruz oil field disaster in 1983 released approximately 1500 barrels of oil daily into the Persian Gulf until the leak was contained months later. Similarly, the 1992 Fergana Valley blowout in Uzbekistan, the largest land-based spill, released 88 million gallons of oil, causing an uncontrollable fire that burned for two months. Marine oil spills, such as the Deepwater Horizon incident in 2010, released 4.9 million barrels of oil into the Gulf of Mexico, causing unparalleled environmental devastation. Oil spills have long posed severe environmental and socio-economic challenges across global marine ecosystems—from the Persian Gulf to Uzbekistan's inland waters and the Gulf of Mexico—causing extensive ecological degradation and substantial economic losses [2]. Historical records highlight several catastrophic incidents that underscore the persistent threat of oil pollution. In the United States, two major events remain particularly significant: the 1969 Santa Barbara oil spill, where an offshore platform blowout discharged approximately four million gallons of crude oil into coastal waters, and the 1989 Exxon Valdez disaster in Alaska's Prince William Sound, which released over 11 million gallons of oil [3]. These large-scale spills not only devastated marine habitats but also catalyzed advancements in environmental policy and spurred the development of oil spill monitoring technologies. Presently, two principal approaches dominate oil spill detection practices [4]. The first involves direct surveillance using maritime assets, such as patrol vessels and stationary sensor buoys, deployed by marine environmental authorities and coastal defense agencies [5–7]. These systems enable real-time observation of sea surface conditions and facilitate rapid data transmission to centralized monitoring centers. Patrol vessels are responsible for on-site inspection and reporting during spill events, while sensor buoys continuously measure and relay oil concentration data from affected areas. However, despite their operational advantages, direct maritime surveillance systems face notable limitations in terms of spatial coverage, mobility, and detection precision. Reaching offshore or remote spill zones can be time-intensive and logistically demanding. Moreover, the restricted field of view from onboard sensors hampers comprehensive situational awareness, particularly in vast or turbulent marine environments. These challenges highlight the critical need for advanced, automated, and scalable oil spill detection methods capable of delivering accurate and timely insights for environmental monitoring.

Conventional monitoring techniques, such as manual inspections and satellite imagery analysis, have traditionally been employed for environmental monitoring and damage assessment. While these approaches may provide reliable information in specific contexts, they are typically resource-intensive and often suffer from delayed data acquisition and processing times. These constraints limit their effectiveness for rapid detection and real-time response in dynamic environments. In contrast, automated detection systems leveraging advancements in deep learning (DL) and computer vision (CV) have demonstrated the potential to transform oil monitoring. The effectiveness of artificial intelligence (AI)—based oil spill detection systems relies heavily on the availability of large, high-quality datasets. However, training DL models to achieve high accuracy necessitates diverse datasets representing a wide array of oil spill scenarios under varying environmental conditions, application of State-Of-The-Art (SOTA) techniques, and DL architectures. For example, current datasets are often limited in both size and scope, leading to models that struggle to generalize in real-world situations. Because oil spills in calm waters appear vastly different

from those in rough seas or polar regions, this necessitates bigger datasets related to varying ocean environmental conditions [8,9].

The main contributions of this study are summarized as follows:

- Development of a custom optical oil spill dataset by integrating blending-based data augmentation techniques that combine source oil spill images with target ocean surface imagery to enhance data diversity and realism.
- Implementation of the SOTA segmentation framework through fine-tuning the YOLOv11m-seg model using the proposed custom dataset.
- LIC method integration to increase ocean wave flow for better object detection and segmentation.

Generation of vector field-based segmentation masks using the LIC approach, where directional flow arrows are aligned with ocean wave dynamics to better represent oil dispersion patterns. In the proposed dataset, oil spill regions are annotated under the class label "Oil in Water" and used for model training.

2. Related Works

Oil spill detection using remote sensing data has been extensively studied over the past few decades, with research broadly categorized into three areas: (1) remote sensing data modalities and their suitability for oil spill characterization, (2) traditional and machine learning ML approaches for spill classification and detection, and (3) DL and CV frameworks for automated segmentation. Each category presents distinct advantages and limitations, which motivate our approach of combining synthetic optical data augmentation, LIC-based flow modeling, and an SOTA segmentation model.

2.1. Remote Sensing Data for Oil Spill Detection

Remotely sensed data, primarily synthetic aperture radar (SAR) and optical imagery, have played a pivotal role in oil spill detection and monitoring over the past few decades. Despite their potential, optical images are less frequently employed than microwave (SAR) imagery due to their reliance on weather conditions and daylight availability. The spectral characteristics of oil spill influenced by factors such as oil type, film thickness, illumination, and water column properties. Congruently, SAR imagery has become the preferred choice for robust oil spill detection across environmental conditions. The use of multi-spectral data for oil spill detection is increasingly prominent, leveraging datasets from satellites like MODIS, Landsat, KOMPSAT-2, and Gaofen-1. These satellite systems offer varied resolutions and capabilities that have been extensively utilized in numerous studies, as can be seen in Table 1.

Table 1. SAR satellite missions and polarization configurations used in oil spill detection studies.

Satellite Name	Operator	Polarization	References
RADARSAT-1	Canadian Space Agency (CSA)	Single-HH	[10–13]
RADARSAT-2	Canadian Space Agency (CSA)	Quad	[14–17]
RISAT-1	India	Quad	[10,12]
Kompsat-5	Korea	Dual	[18,19]
Sentinel-1	European Space Agency (ESA)	Dual	[18–21]

Recent research has further explored the use of near-infrared spectral (NIR) bands, ranging from 750 to 1400 nm, in sun-glittered satellite imagery for oil spill identification. Adamo et al. [22] found that NIR bands from MODIS and Medium Resolution Imaging Spectrometer (MERIS) imagery were more effective at distinguishing oil from non-oil areas than bands in the visible spectrum. This finding highlights the superior performance of NIR

and SWIR spectral ranges in improving the precision and reliability of optical methods for oil spill detection. Perez et al. [23] investigated the effectiveness of the fluorescence index (FI) and the rotation-absorption index (RAI), which utilize the fluorescence characteristics of oil slicks. These methods were tested using hyperspectral optical imagery from the 2010 Deepwater Horizon oil spill. Their findings demonstrated that optical imagery could reliably distinguish oil slicks from radar-detected false positives, particularly in conditions with low wind speeds. This methodology enabled precise mapping of oil spill extent and thickness, highlighting the potential of infrared imaging for oil slick detection when applied to Moderate Resolution Imaging Spectroradiometers (MODIS) data. Similarly, Dubucq et al. [24] highlighted the efficacy of near-infrared (NIR) and short-wave infrared (SWIR) multispectral data for detecting oil slicks. The FI index relies on reflectance values from the blue and red bands, while the RAI formula incorporates reflectance from the blue, infrared, and i-th bands. For Landsat OLI imagery, the SWIR characteristics were calculated by averaging reflectance values from band 6 (1609 nm) and band 7 (2201 nm). For Terra MODIS imagery, the SWIR spectral characteristics were derived similarly, using band 6 (1640 nm) and band 7 (2130 nm). The key spectral indices used in oil slick detection are summarized in Table 2.

Table 2. Oil slick detection spectral indices.

Indices	Formulas		References
FI	$FI = \frac{R_S - R_R}{R_S + R_R}$	(1)	[24]
RAI	$RAI = \frac{R_S - R_R}{R_S + R_R} \sqrt{\sum b_i^2}$	(2)	[24,25]
SWIR	$SWIR_{OLI} = 0.5 * (R_{B6} + R_{B7})$	(3)	[26,27]
	$SWIR_{MODIS} = 0.5 * (R_{B6} + R_{B7})$	(4)	

2.2. Traditional Monitoring and Classical Machine Learning Methods

Conventional approaches to detecting and monitoring marine oil spills—including satellite imagery, aerial surveillance, and manual onsite reporting—continue to hold significant importance in this domain [28]. Historically, onsite monitoring was the primary approach for oil spill detection. While these traditional methods provided direct and immediate observations, they posed considerable challenges, including exposure to hazardous substances and other safety risks during field operations. To address these limitations, various ML models have been developed to tackle complex classification problems. These models utilize recursive training processes to improve detection accuracy. Prominent ML algorithms applied in oil spill detection include SVM [29], Decision Trees (DT) [30], KNN [31], Random Forest (RF) [32], and others. Each algorithm offers unique advantages and limitations, depending on the nature and complexity of the data. Building on these datasets, machine learning (ML) models have been developed to enhance detection capabilities and distinguish oil spills from lookalike phenomena. These ML models capitalize on both optical and SAR data to provide efficient and scalable solutions. ML approaches to oil spill detection can be broadly classified into traditional techniques and DL methods. Traditional ML models, such as artificial neural networks (ANN), support vector machines (SVM), k-nearest neighbor (KNN), and random forest (RF), have demonstrated effectiveness in processing optical and SAR imagery for oil spill detection. For instance, Yu et al. [33] proposed a hybrid method combining region generation, edge detection, and threshold segmentation, which was enhanced by an adaptive mechanism based on the Otsu method. In CV and image processing, the Otsu method is mostly used for automatic image thresholding purposes. Validated using SAR data from the Bohai Sea and Danian Bay, their approach showcased robust detection performance. Similarly, Zhang et al. [34] introduced a method for mapping oil spills in the Gulf of Mexico by calculating the confor-

mity coefficient from fully polarimetric SAR data. In their approach, researchers optimized the low to medium wind speeds, demonstrated high accuracy, emphasizing the value of polarimetric data in oil detection. Del Frate et al. [35] pioneered the use of multi-layer perceptron (MLP) neural networks with SAR imagery for oil spill recognition, achieving promising results that underscored the potential of neural networks in this domain. Chen et al. [36] further advanced SAR-based detection by designing a novel convolutional architecture, A-ConcNets, to address overfitting issues, enhancing the generalizability of SAR image classification. Feature extraction remains a critical component in oil spill detection, enabling the differentiation of oil spills from similar phenomena like algal blooms, biogenic slicks, and low-wind regions. By incorporating features with high discriminatory power, ML models achieve improved accuracy in identifying spills. Traditional approaches to feature extraction often involve manually engineered algorithms. Xu et al. [37] utilized the Otsu algorithm for image segmentation, enabling the separation of oil spill regions from surrounding water by optimizing thresholds that minimize intra-class variance. Researchers said that Hasan et al. [38] conducted a comparative analysis of three widely used supervised classifiers, including ANN and SVMs, for classifying oil spills in synthetic aperture radar imagery. While SVMs are particularly suited for binary classification tasks, their performance in handling complex, non-linear data is inherently limited. To overcome this, the concept of kernel was introduced, allowing SVMs to map input data into higher-dimensional feature spaces. This transformation facilitates the construction of optimal separating hyperplanes, enabling the effective handling of non-linear decision boundaries. Several kernel functions have been developed for SVMs to address diverse data complexities, including linear, polynomial, sigmoid, and radial basis function (RBF) kernels. In the context of oil spill classification, RBF and polynomial kernels are particularly favored for their capabilities to capture the nonlinear pattern characteristics of remote sensing and marine environments [39,40]. The selection of an appropriate kernel and its parameters is critical for achieving high classification accuracy. Moreover, these traditional surveillance techniques can be limited by weather conditions, operational logistics, and the delay in real-time data transmission, highlighting the need for more advanced and cost-effective remote sensing technologies.

2.3. Deep Learning and Computer Vision Approaches

The application of CV and DL techniques has significantly advanced automated oil spill detection. Jiao et al. [1] employed a deep CNN to improve the accuracy of oil spill detection. Their approach enhanced the standard CNN architecture by introducing an additional convolutional layer, along with a fully connected layer, to improve feature extraction and classification performance. The input data comprised images collected via Unnamed Aerial Vehicles (UAVs), supplemented with metadata such as GPS coordinates, pitch angle, and other relevant parameters, which provided contextual information for better detection accuracy. The study results demonstrated the robustness of the model, achieving an impressive 99.33% accuracy in mAP, highlighting its potential applicability for real-world oil spill detection tasks. Moreover, the researchers addressed the issue of overfitting, a common challenge in DL models, by incorporating techniques such as optimized dropout rates and L2 norm regularization. Similarly, De Kerf et al. [41] introduced a methodology leveraging both visible and infrared imagery captured by UAVs to facilitate oil spill detection at night. Their experimental setup simulated a controlled oil spill in a small but realistic seaport environment, where UAVs equipped with cameras were used to capture both visible and infrared image data. The research focused on training a model by combining various backbone architectures with segmentation networks. After extensive experimentation, the team found that the most effective oil detection model for nighttime conditions utilized

the MobileNet backbone integrated with the fully convolutional network with an 8-pixel (FCN8) segmentation. This model achieved an impressive 89% mean Intersection over Union (mIoU) in their experimental context. Reported accuracies of SVM models in oil spill detection studies vary significantly, ranging from 71% to 97%. This variation underscores the potential of SVMs while highlighting the importance of proper model tuning, such as optimizing hyperparameters and kernel selection, to enhance their performance. By addressing these considerations, SVMs can serve as powerful tools for oil spill classification tasks, particularly when integrated with robust preprocessing and feature extraction techniques. These models have been applied to a variety of tasks, including oil spill detection and recognition [42–44], determining their versatility in tackling different challenges in the field. Notably, they have been utilized for tasks such as image patch-based classification, where images are divided into smaller patches for detailed analysis and semantic segmentation, which involves the pixel-level classification of an image to precisely identify oil spill regions. To improve detection and response capabilities, ocean surveillance systems, incorporating the use of aircraft and coastguard forces, were subsequently introduced.

3. Proposed Method

3.1. Dataset Description

Numerous studies have demonstrated the benefits of data augmentation in ML for training DL models. The performance of ML models, particularly in CV tasks, is closely tied to the quality and quantity of the training data. It is well established that larger datasets generally lead to better-performing DL models. Initially, we collected original oil spill images from publicly available sources. Our model development is oriented to CV. We collected RGB oil spill images from various ocean environments. However, there are limitations related to oil spill images in various maritime environments. Therefore, we collected original ocean images, where no oil spill is represented. After this collection process, we applied augmentation techniques to create synthetic oil spill images to increase our dataset size and to improve the proposed model's detection accuracy. Figure 1 below represents how we create synthetic oil spill images by blending an original oil spill image into various ocean images. We focused on different ocean conditions, such as rainy, snowy, wavy, etc., to feed the vision model to better recognize oil spills.

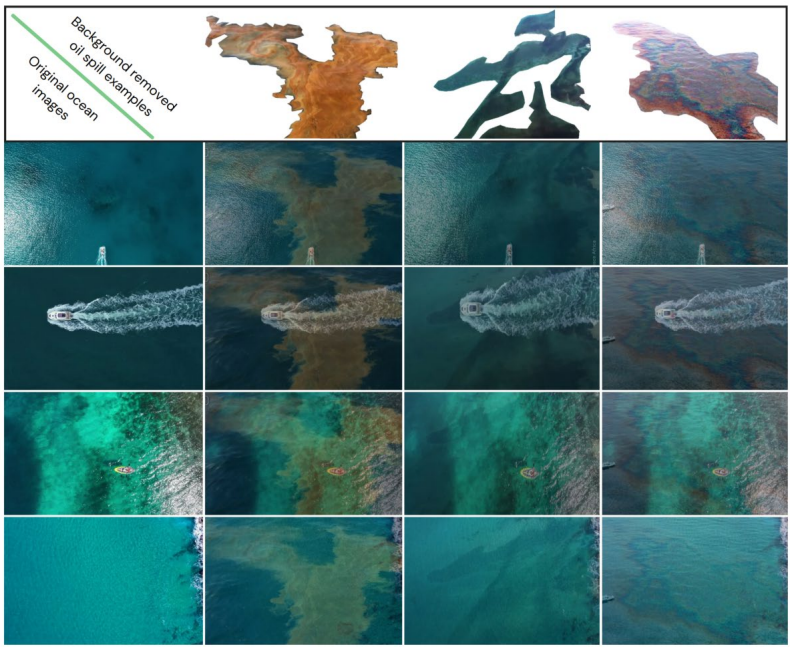

Figure 1. Oil spill dataset creation from blending source (ocean) and target (oil spill) images.

Data preprocessing steps include background removal from target images and applying rotation, flipping techniques, while blending with the source image. After removing the background from the target image, we label this image as "Oil in water", where the model recognizes these regions as oil representation in the ocean. Figure 2 highlights examples of "Oil in water" oil spills as extracted background. Those target images are combined with source images.

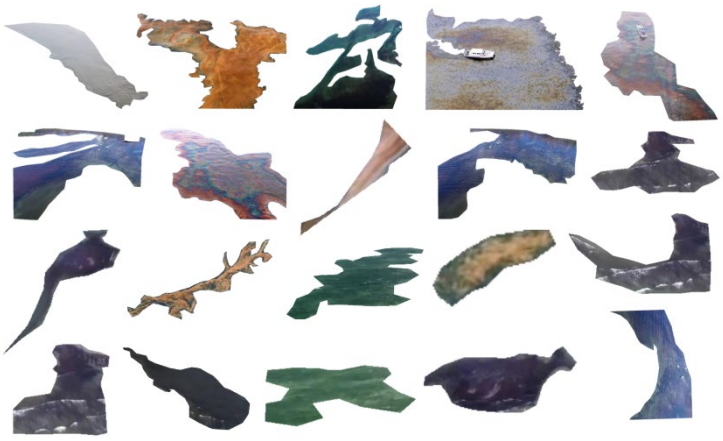

Figure 2. Examples of target (oil spill) images.

Figure 3 illustrates the relationship between oil slick thickness and its visual appearance in marine environments. When the oil film is extremely thin (approximately 0.05–0.2 nm), it appears silvery due to surface reflection dominating over absorption, predicting a metallic sheen commonly classified as silver sheen. At intermediate thickness (0.3–3 nm), thin-film interference becomes significant, causing wavelength-dependent constructive and destructive interference that generates a characteristic rainbow coloration.

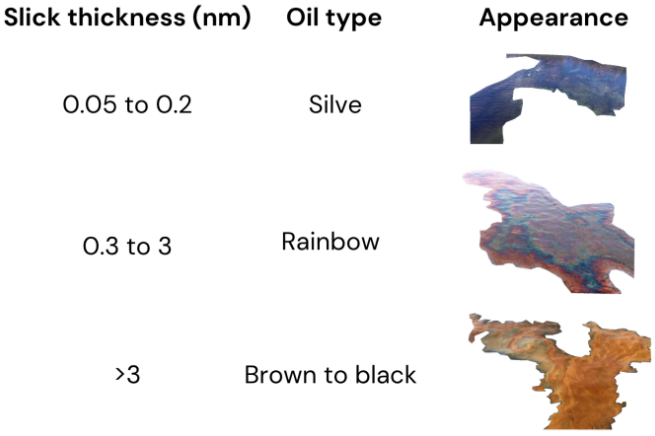

Figure 3. Oil spill types, appearance, and thickness details.

When the slick thickness exceeds 3 nm, the oil layers become brown to black in appearance. This thickness-dependent optical behavior is fundamental in oil spill detection, as it influences spectral reflectance properties and radar backscatter responses, thereby supporting remote sensing-based classification.

3.2. Line Integral Convolution (LIC) Application for Estimation of Wave Flow in Ocean

LIC is a technique used to visualize vector fields, often applied to flow-like phenomena, such as fluid dynamics, weather patterns, or image analysis tasks like oil spill detection.

In our approach, LIC is used to visualize the flow of detected oil spill regions in an image following the gradient field and generating a texture along the flow lines (Figure 4).

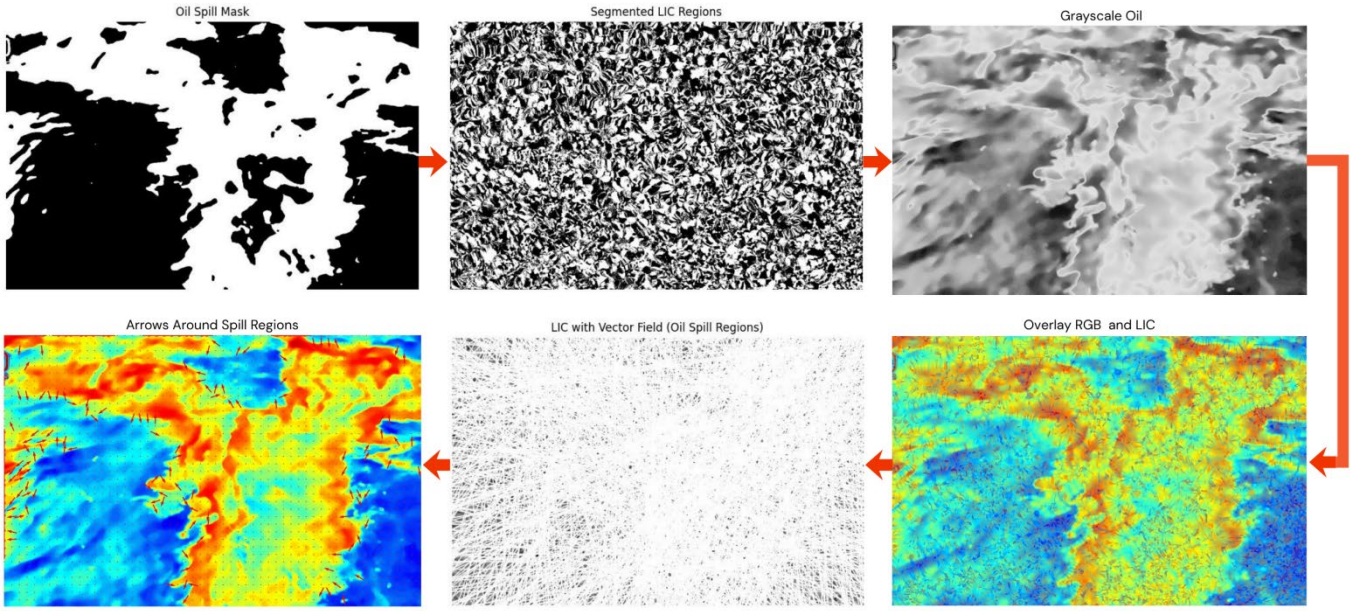

Figure 4. The LIC application processes for the estimation of wave flow in the ocean and to surround spill regions with arrows. The process starts from the oil spill label region and the LIC segmentation of this region to create predictive vector fields. Grayscale channels of the oil spill are also created before overlaying the LIC on the oil spill mask. All these steps help to improve the arrow localization in the spill regions.

From the mathematical description, we can adapt the formal description of the LIC process to visualize the vector field generated from the oil spill regions. The goal is to represent the flow direction and intensity of the detected oil spill, which can be treated as a vector field. This field can be used to reveal the underlying flow patterns, providing a deeper understanding of how the oil spill evolves in the image domain.

3.3. Vector Field Representation in the Image

As described, let's consider v to be the vector field in the image domain Ω, where the domain Ω corresponds to the pixel space of the image that contains the oil spill and its surrounding environment. Although the vector field is discretized in the image, we treat it as a continuous Ω, interpolating at every point. The vector field $v(x,y)$ is derived from the image gradient, as described in the previous sections, and represents the direction and intensity of the vector field at each pixel. The oil spill is detected through segmentation, where the boundaries and flow directions are important in understanding the nature of the spill. The streamlines or field lines, in general, are the trajectories that are tangent to the vector field at each point in the image. These trajectories represent the potential flow paths of the oil spill, and they will either end at the boundaries of the image or at critical points.

3.4. Field Line and Parametrization

Considering a field line σ, parameterized by arc length s, that describes the flow direction along the vector field. The field line is defined by the differential equation:

$$\frac{d\sigma(s)}{ds} = \frac{v(\sigma(s))}{|v(\sigma(s))|}, \tag{5}$$

where $\frac{d\sigma(s)}{ds}$ is the tangent to the field line at each point, $v(\sigma(s))$ is the vector field at the point $\sigma(s)$ and $|v(\sigma(s))|$ is the magnitude of the vector field at the point $\sigma(s)$.

The field line $\sigma_r(s)$ stands from an initial point r (the pixel r in the image) at $s = 0$, represents the oil spill's flow direction starting from that pixel.

3.5. Convolution Along the Field Line

At each pixel r, the intensity $D(r)$ of the resulting LIC image is computed by integrating a convolution of the noise texture $N(\sigma_r(s))$ along the field line $\sigma_r(s)$, as it is traced through the vector field. The integral is expressed as:

$$D(\mathrm{r}) = \int_{-L/2}^{L/2} k(s) \cdot N(\sigma_r(s)) \cdot ds, \tag{6}$$

where $k(s)$ is the convolution that modulates the contribution of the noise at each point along the field line. $N(\sigma_r(s))$ is the value of the noise texture at the point $\sigma_r(s)$ on the field line, and L is the total length of the segment of the field line being traced in the input oil spill image. The kernel function $k(s)$ is usually designed to smooth the contribution from nearby points, so points to the current pixel r contribute more significantly to the final image intensity than points farther away.

To compute $D(r)$ for every pixel in the LIC image, the streamlines must first be traced using a numerical method for solving ordinary differential equations, such as the Runge–Kutta method. This method integrates the vector field along each streamline from the pixel r, producing the path of the streamline. Once the streamline is computed, the convolution along the streamline is performed, integrating the noise texture along the path, weighted by the kernel $k(s)$. This step is computationally intensive, as it requires evaluating the field lines and performing convolutions for each pixel in the image. However, once computed, the LIC can reveal the flow patterns of the oil spill, where brighter regions correspond to areas with stronger flow, and the texture of the image represents the dynamics of the spill. The convolution process adds a smoothing effect, producing an image where the oil spill flow is visually connected across the image domain. Finally, once the grayscale LIC output is computed, we map the color scale to highlight different features of the vector field. A scalar field, such as the vector magnitude $|\mathrm{v(x,y)}|$, can be used to color the final image. In that stage, higher magnitudes, which represent stronger flow, might be represented with warmer colors, and weaker flow regions might be represented with cooler colors. In our case, the final color mapping helps to visually distinguish between areas of high and low oil spill activity, providing an intuitive representation of how the spill is spreading across the ocean.

4. Mathematical Application for Improving Oil Spill Extraction

4.1. Gradient Field Computation

The function computes the gradient field using the Sobel operator. The gradient field represents the rate of change in pixel intensities in the horizontal and vertical directions.

Gradient along x-axis (horizontal):

$$\nabla_x = Sobel(I, 1, 0, k), \tag{7}$$

Gradient along y-axis (vertical):

$$\nabla_y = Sobel(I, 1, 0, k), \tag{8}$$

where I is the input grayscale image, k is the kernel size.

The magnitude (M) of the gradient is normalized:

$$M = \sqrt{\nabla_x^2 + \nabla_x^2} + \epsilon, \tag{9}$$

$$\nabla_x' = \frac{\nabla_x}{M}, \nabla_y' = \frac{\nabla_y}{M}, \tag{10}$$

The computation of the gradient field serves as a foundational step in enhancing the extraction of oil spill regions from oceanic imagery, as it effectively highlights edges and regions of intensity variation corresponding to the boundaries of oil patches. In this process, the Sobel operator is employed to calculate the spatial rate of change in pixel intensities in both horizontal (G_x) and vertical (G_y) directions. Mathematically, G_x captures the gradient along the x-axis, emphasizing vertical and horizontal transitions, while G_y measures the gradient along the y-axis, emphasizing vertical transitions. These gradients are computed by convolving the grayscale image I with Sobel kernels of size k, producing directional derivatives that accentuate edges where oil spill textures differ from surrounding water surfaces. The overall gradient magnitude M is then derived as the Euclidean norm of these components, typically expressed as:

$$M = \sqrt{G_x^2 + G_y^2 + \epsilon}, \tag{11}$$

where ϵ (a small constant such as 10^{-5}) ensures numerical stability by preventing division by zero during normalization.

4.2. Line Integral Convolution (LIC)

LIC visualizes vector fields (gradients) by pixel intensity along streamlines of the vector field (∇_x, ∇_y).

Given:

- (p_x, p_y): The starting pixel coordinates.
- $v_x = \nabla_x(p_x, p_y), v_y = \nabla_y(p_x, p_y)$: Normalized gradient directions.

The LIC technique is applied to visualize the flow dynamics of oil spill regions by representing the local vector field—derived from image gradients—as continuous textures aligned with the direction of motion. In this process, each pixel is treated as a potential starting point within the domain, from which a streamline is traced following the normalized gradient direction. This direction indicates the local flow orientation of oil spill textures relative to the surrounding ocean surface.

Initialization of LIC Integration Parameters

$$I_{sum} = 0, w_{sum} = 0, \tag{12}$$

Integrate pixel intensities along the streamline in both positive and negative directions over a kernel length L:

$$I_{sum} + = I(x_k, y_k) \cdot \left(1 - \frac{|k|}{L}\right), w_{sum} + = \left(1 - \frac{|k|}{L}\right), \tag{13}$$

where (x_k, y_k) is the pixel reached by advancing along the gradient direction:

$$x_{k+1} = x_k + v_{x,} y_{k+1} = y_k + v_y, \tag{14}$$

Normalize the output:

$$\mathrm{LIC}(p_{k,} p_y) = \frac{I_{sum}}{w_{sum}}, \tag{15}$$

The result is then normalized to [0, 255] for display.

The LIC algorithm operates by integrating pixel intensities along these streamlines, effectively convolving the underlying image intensity with a filter kernel over a specified length L. The final step involves normalizing the LIC output to a range of [0, 255], ensuring consistent visualization across varying illumination and intensity scales to effectively reveal the flow behavior and spatial distribution of detecting oil spill regions. The Laplacian operator enhances edge structures by calculating the second derivatives:

$$\text{Laplacian}(I) = \frac{\delta^2 I}{\delta x^2} + \frac{\delta^2 I}{\delta y^2}, \tag{16}$$

The image is enhanced by adding a scale Laplacian back to the original:

$$I_{enhanced} = |I + a \cdot \text{Laplacian}(I)|, \tag{17}$$

where $a = 0.7$ is a scaling factor.

4.3. Combining Results

Finally, the processed components are combined into a multi-channel image:

$$I_{combined} = Stack\left(I_{brightened}, E, LIC\right), \tag{18}$$

where

- $I_{brightened}$ is the gamma-corrected image
- E is the combined edge map
- LIC is the integral convolution map.

This output $I_{combined}$ gives us the enhanced features of oil spill regions for better region extraction for segmentation and further analysis (Figure 5).

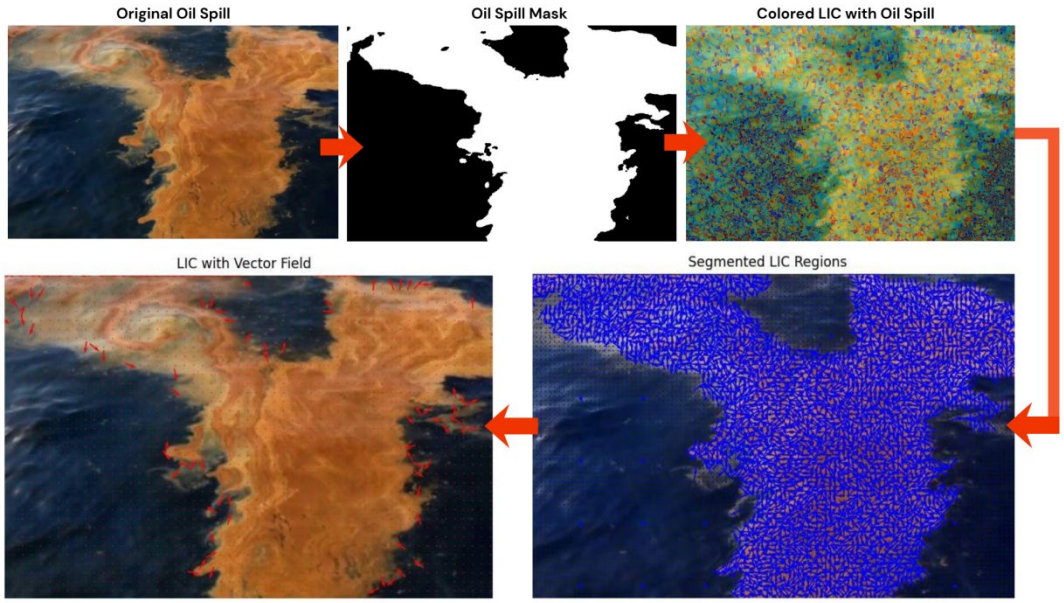

Figure 5. Workflow of oil spill flow visualization and segmentation using LIC. The process includes the original oil spill image, binary spill mask generation, colored LIC visualization, segmented LIC regions, and vector field overlay. This step of the visualization methods enhances structural and directional feature extraction for improved spill pattern analysis.

Figure 5 illustrates the complete processing pipeline for analyzing oil spill dynamics through LIC-based flow visualization and segmentation. The workflow effectively captures both the spatial distribution and direction behavior of oil slicks on the ocean surface, integrating texture information and vector field representation for precise motion characterization. The process begins with the original oil spill image (top-left), which depicts the natural spatial distribution and visual complexity of the spill region, including color gradients, surface reflections, and dispersion boundaries. From this image, an oil spill mask (top-middle) is generated to isolate the contaminated region from the surrounding ocean background. This binary mask is crucial for removing background noise and focusing subsequent analysis exclusively on oil-covered areas.

The masked region is then processed through LIC with oil spill (top-right), which visualizes the underlying texture flow field by mapping vector orientations onto a noise texture convolved along streamlines. This representation reveals subtle spatial correlations and anisotropic flow directions that are not visible in raw imagery. The resulting LIC visualization accentuates surface streaks and oil dispersion trajectories, providing a deeper understanding of hydrodynamic behaviors influenced by currents and wind patterns. Next, the segmented LIC regions (bottom-right) display the output of segmentation algorithms applied to the LIC representation. These regions (highlighted in blue) delineate coherent flow patterns and visually distinct oil clusters. The segmentation step transforms complex flow textures into quantifiable regions, facilitating feature extraction for downstream ML or physical modeling tasks. Finally, the LIC with vector field visualization (bottom-left) overlays the computed velocity onto the oil spill image, illustrating both the magnitude and direction of surface motion. The red arrows indicate localized flow vectors, revealing the movement tendencies of oil patches and boundary instabilities. The vector alignment with the LIC streamlines confirms the consistency of the extracted motion field and validates the accuracy of the computed flow map. The integrated LIC-based analysis enables a multidimensional understanding of oil spill behavior—combining intensity, flow orientation, and structural segmentation. By capturing fine-grained motion textures and spatial coherence, this framework supports improved detection, segmentation, and predictive modeling of oil dispersion in dynamic marine environments, offering valuable insights for environmental monitoring and emergency response planning.

5. Experimental Results and Analysis

5.1. Model Training

We used yolo11m-seg.pt for model training with our developed custom dataset by integrating the LIC algorithm to detect oil spills in ocean environments. The YOLOv11-seg model is a medium-scale pre-trained instance segmentation network from the YOLOv11 family developed by Ultralytics. Architecturally, it follows a one-stage detection paradigm composed of a convolutional backbone for hierarchical feature extraction, a neck (typically PAN/FPN-style feature aggregation) for multi-scale feature fusion, and a segmentation head that jointly predicts bounding boxes, class probabilities, and pixel-wise object masks. Given an input image $I \in R^{H\times W\times 3}$, the network learns a nonlinear mapping $f_\theta(I) \rightarrow \{(b_i, c_i, m_i)\}_{i=1}^{N}$, where b_i denotes bounding box coordinates, c_i class confidence scores, and m_i segmentation masks. The training objective generally combines bounding box regression loss, classification, and mask loss, forming a composite loss. For fine-tuning, enriched LIC-based ocean oil spill imagery, the pre-trained model enables transfer learning to accelerate convergence and to improve the segmentation of the oil spill region in ocean environments. In Table 3, we included proposed model training parameters and dataset description.

Table 3. Summary of oil spill dataset and experimental hyperparameters.

Attribute/Parameter	Description
Data source	Google images, public YouTube videos
Scene types	Ocean, oil spills
Ocean scenes	Open sky/cloudy/rainy/foggy
Oil spill type	Crude oils/Refined oils/Medium oils/Heavy oils
Spill characteristics	Surface oil
Total images	18,136
Dataset split (Train/Val)	80%/20%
Training images	14,508
Validation images	3627
Input resolution	$640 \times 640 \times 3$
Backbone	Cross-Stage Partial Networks
Optimizer	Adam
Initial learning rate	Le-5
Classes name	"Oil in water"
Annotation tool	Makesenseai(polygon)
Annotation format	Yolo txt (csv)
Framework compatibility	PyTorch (version 12.6)
Number of epochs	50

Our proposed framework integrates LIC-based structural enhancement with a pre-trained yolo version. First, the input image is transformed into a normalized gradient vector field using Sobel operators, where spatial derivatives are computed as $G_x = \delta I/\delta x$ and $G_y = \delta I/\delta y$. The unit vector field is defined as:

$$\vec{V}(x,y) = \left(\frac{G_x}{\sqrt{G_x^2 + G_y^2 + \epsilon}}, \frac{G_y}{\sqrt{G_x^2 + G_y^2 + \epsilon}} \right), \tag{19}$$

ensuring direction preservation independent of magnitude. LIC is applied by convolving a random noise texture $N(x,y)$ along streamlines governed by $\vec{V}(x,y)$, such that the LIC response at pixel $(x_0 y_0)$ is expressed as:

$$L(x_0 y_0) = \frac{1}{W} \sum_{s=-k}^{k} N(\boldsymbol{p}(s) w(s)), \tag{20}$$

where $\boldsymbol{p}(s)$ represents streamline coordinates. $w(s) = 1 - |s|/k$ is a linear kernel for weighting. The resulting LIC texture map, which enhances flow-align structural patterns and edge continuity, is concatenated with the original RGB image to form an enriched multi-channel representation. The integration of LIC-derived texture features aims to improve boundary sensitivity and segmentation accuracy, particularly for oil spill detection. Figure 6 presents qualitative detection results of an oil monitoring model, where multiple marine images are annotated with bounding boxes labeled "Oil in water".

Each sub-image illustrates different oceanic scenarios, including open sea conditions, nearshore coastal environments, vessel-associated discharges, and heterogeneous background textures such as waves, sediment plumes, and shoreline features. The model is trained for 50 epochs, and this figure is a representation of labeled oil spill regions. The detected oil regions exhibit varying geometries, including long gated streaks, diffuse patches, and large continuous surface films, reflecting the dynamic spreading behavior of hydrocarbons under wind and current forcing. Overall, the visualization evidences the robustness of the trained detection framework in capturing multi-scale oil slick structures in diverse marine contexts.

Figure 6. Qualitative visualization of oil spill detection results in diverse marine environments.

5.2. Evaluation Metrics

The evaluation metrics (Table 4) are used to quantitatively measure the reliability, robustness, and practical applicability of the proposed method for the oil spill detection model.

Table 4. Evaluation metrics to calculate the performance of the proposed model.

True Positive (T_P)	The number of instances correctly identified as belonging to the positive class.
True Negative (T_N)	The number of instances correctly identified as not belonging to the positive class.
False Positive (F_P)	The number of instances incorrectly identified as belonging to the positive class.
False Negatives (F_N)	The number of instances that belong to the positive class but were not recognized as such by the model.
mean Average Precision (mAP@0.50:0.95)	mAP is a ranking measure that evaluates the quality of a rank.

In environmental monitoring tasks such as marine oil spill detection, simple accuracy alone is insufficient because the dataset is often imbalanced (large background water areas versus relatively small oil slick regions). Therefore, Precision is essential to assess the proportion of correctly identified oil regions among all predicted oil detections, minimizing false alarms that could lead to unnecessary response operations. Recall is equally critical, as it measures the model's ability to detect actual oil-contaminated areas, reducing missed spills that could cause severe environmental damage. The F1-score, as the harmonic mean of the precision and recall, provides a balanced assessment when both F_P and F_N are significant. Accuracy offers an overall correctness measure but must be interpreted cautiously in imbalanced scenarios. mAP is a stricter metric that evaluates localization accuracy, as it requires accurate boundary delineation across multiple overlap thresholds, which is particularly relevant for oil spill segmentation, where precise mask boundaries are critical for spill volume estimation.

$$Precision = \frac{T_P}{T_P + F_N}, \tag{21}$$

$$Recall = \frac{T_P}{T_P + F_P}, \tag{22}$$

$$F_1 - score = \frac{2T_P}{2T_P + F_P + F_N}, \tag{23}$$

$$mAP = \frac{1}{n}\sum_{k=1}^{k=n} AP_k, \tag{24}$$

Collectively, these metrics ensure a comprehensive evaluation of detection performance, enabling objective comparison between models and supporting the development of a reliable decision-support system for real-world oil spill surveillance and environmental risk management.

Figure 7 shows the training performance curves of the fine-tuning YOLO11m-seg model with our proposed approach over successive epochs, presenting evaluation metrics for both bounding box detection (B) and segmentation mask prediction (M). The blue line is the individual per-epoch metric value recorded on the validation set, and the orange dots are the exponential moving average smoothed trend curve over all epochs. This smoothing is applied to reduce epoch-level noise and reveal the overall convergence trend more clearly. The upper row shows precision and recall trends, where both metrics exhibit a rapid increase during the initial training epochs followed by gradual stabilization, indicating effective convergence and improved classification reliability. Precision approaches a value close to 1.0 for both bounding boxes and masks, suggesting a low false-positive rate, where recall stabilizes above 0.9, reflecting strong sensitivity in detecting oil spill instances.

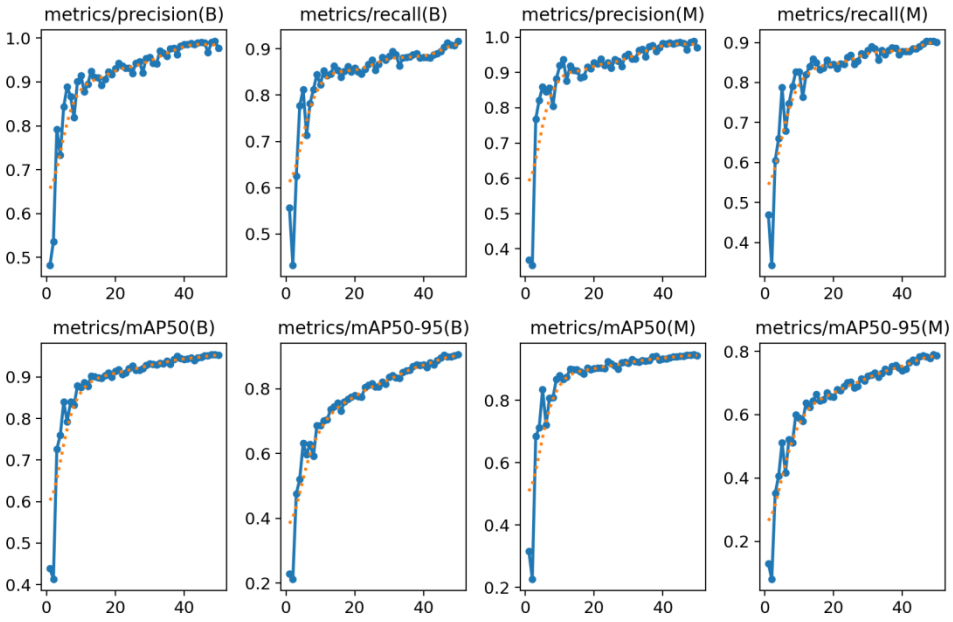

Figure 7. Training performance curves of the fine-tuned YOLOv11m-seg over 50 epochs. Each subplot displays the per-epoch metric values recorded on the validation set (blue lines) and the corresponding exponential moving average smoothed blue line. The upper row shows bounding box precision (B-Precision) and recall (B-Recall), and mask precision (M-Precision) and recall (M-Recall). The lower row presents mAP@0.50 and mAP@0.50:0.95 for both bounding box (B) and segmentation mask (M) prediction tasks. The rapid initial improvement followed by stable convergence confirms effective model learning and the absence of overfitting.

The lower row presents mean Average Precision (mAP) metrics, including mAP@0.50 and mAP@0.50-0.95 for both detection and segmentation tasks. The mAP@0.50 curves demonstrate high performance (above 0.90 for bounding boxes and slightly lower for masks), whereas mAP@0.50-0.95, which evaluates performance across multiple IoU thresholds, shows steady improvement and convergence around robust values, indicating accurate localization and mask delineation under stricter optimization, effective feature

learning, and strong generalization capability of the trained model for oil slick detection and segmentation.

6. Discussion

Figure 8 represents the key performance metrics of the proposed YOLOv-11m-seg-based oil spill segmentation model, evaluated across precision-confidence, recall-confidence, F1-confidence, and precision-recall curves. These plots collectively characterize the trade-off between detection confidence and classification accuracy, serving as a comprehensive assessment of the model's learning stability and detection reliability. The precision-confidence curve (top-left) demonstrates a rapid increase in precision as confidence rises from 0.0 to 0.3, followed by a stable plateau approaching > 1.0 precision beyond a confidence threshold of approximately 0.924. This indicates that the model effectively minimizes false positives at higher confidence levels. Confirming its strong discriminative capability in differentiating oil spill regions from non-spill ocean surface. Such performance is crucial in real-world monitoring applications where false alarms can lead to inefficient resource deployment. Similarly, the recall-confidence curve (top-right) shows a gradual increase in recall confidence, stabilizing around 94% accuracy levels. This behavior reflects the model's ability to maintain high sensitivity in detecting true oil spill instances while illustrating the expected trade-off—where higher confidence thresholds yield fewer detections but greater certainty in prediction. F1-confidence curve (bottom-left) indicates both precision and recall to evaluate the model's harmonic balance between sensitivity and specificity. The curve achieves a peak F1 score of approximately 0.94 at a confidence threshold near 0.3, highlighting an optimal operational range for balanced detection.

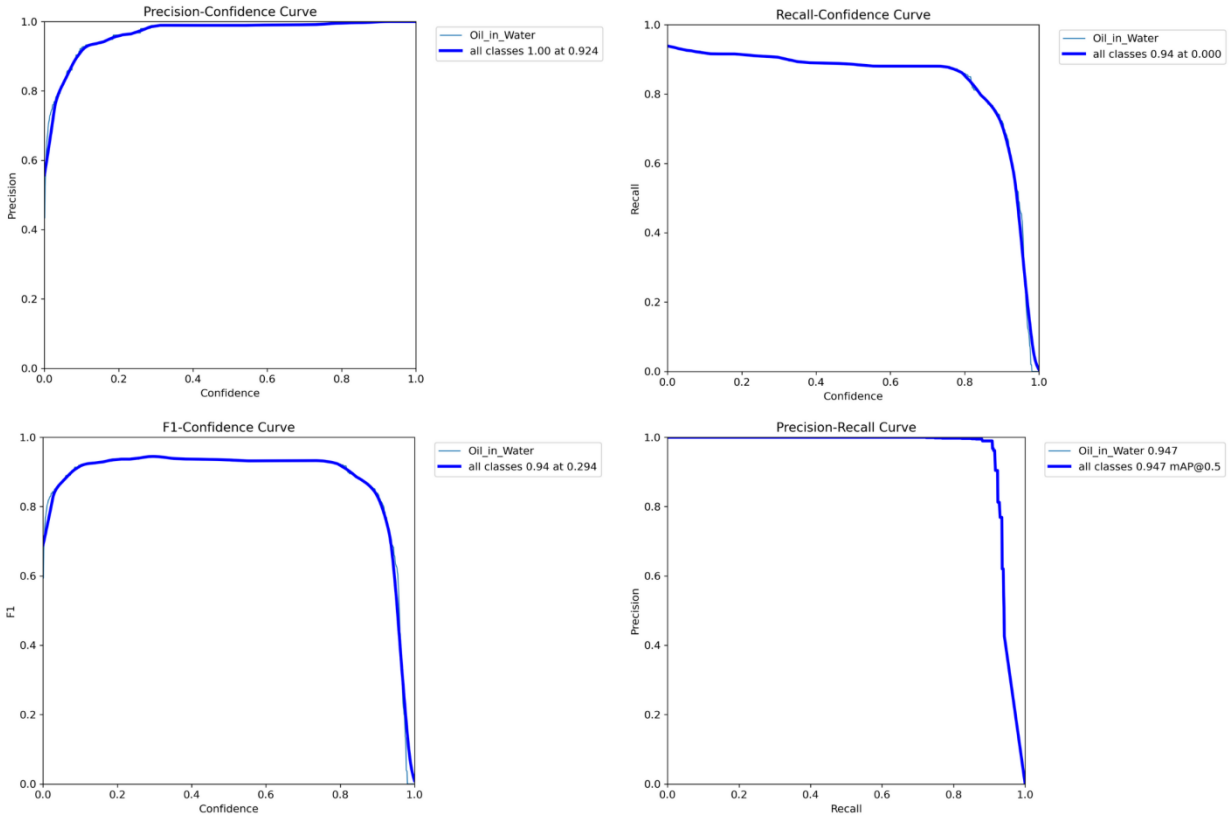

Figure 8. Model performance evaluation curves for oil spill segmentation.

The wide plateau observed across confidence values between 0.3 and 0.8 indicates consistent model robustness and generalization capability, essential for deployment in

dynamic marine conditions with varying illumination, wave patterns, and reflection effects. Finally, the precision-recall (bottom-right) further validates the model's strong predictive consistency, maintaining precision values above 0.9 across nearly the entire recall spectrum. The area under the precision-recall curve (AUC ≈ 0.947) and mAP@0.50 score of 0.947 collectively affirm the model's superior segmentation performance. This high mAP value signifies that the model successfully identifies and delineates oil spill regions with minimal overlap error and accurate boundary localization.

The table presents a quantitative comparison between the proposed oil spill detection approach and the method reported by De Kerf et al. [41] for oil spill detection in ocean images.

Our proposed method demonstrates superior performance across all evaluation metrics. Specifically, it achieves an F1-score of 0.94 (at confidence ≈ 0.924), significantly higher than 0.72. Similarly, other comparative metrics also showed greater scores if we compare our oil spill detection model with [41]. In Table 5, we have compared our proposed model achievements with SOTA U-Net, E-Net, and DeepLabV3 models, in the context of pixel-based oil spill detection in ocean environments. The proposed approach achieves the highest mIoU of 94.74%, substantially outperforming U-Net (86.33%), E-Net (79.52%), and DeepLabV3 (89.58%), indicating superior segmentation accuracy and boundary delineation of oil spill regions.

Table 5. Quantitative comparison table for performance metrics of "Oil in water" with De Kerf et al. [41], segmented RGB images for oil spill detection.

	Our Proposed Approach		**De Kerf et al. [41]**
F1-score	0.94	Confidence ≈ 0.924	0.72
Precision	>1.00	Confidence ≈ 0.000	0.77
Recall	0.94	Peak F1 at confidence ≈ 0.294	0.79
IoU@0.50 (IoU = 0.50)	0.947	Area under Precision-Recall	0.69
IoU@0.50-0.95 (Mean IoU)	~0.80–0.85	Training results	

In terms of precision and recall, the proposed method attains approximately 94.0% (at a confidence threshold of 0.294) and 94.0%, respectively, reflecting a balanced ability to minimize F_P while effectively detecting true oil spill areas. Consequently, the F1-score reaches 94.0%, surpassing all comparative models, with DeepLabV3 being the closest competitor at 91.72%. Overall, the table demonstrates that the proposed framework provides improved robustness, localization accuracy, and detection reliability for oil spill segmentation in marine environments.

The proposed framework achieves mIoU (94.7%) and mAP@0.50 among all compared methods, as highlighted in Table 6. Against classical segmentation architectures, our approach outperforms DeepLabV3 by +5.12% mIoU and U-Net by +8.37% mIoU. It is important to note that SOTA methods operating on SAR data (e.g., Li et al. [28], 88.4% mIoU; Chen et al. [36], 91.2% mIoU) are not directly comparable as they exploit different modality-specific features. Nevertheless, the proposed optical approach achieves comparative or superior mIoU even relative to these SAR-based approaches, which benefit from all-weather imaging capability, while our approach operates on visually rich optical imagery with higher interpretability which can be seen in Tables 6–8 below.

Table 6. Ablation study of the proposed approach.

Configuration	mAP@0.50	mAP@0.50:0.95	F1-Score	mIoU
Baseline (real data)	0.83	0.71	0.85	0.81
+Synthetic data (no LIC)	0.91	0.79	0.91	0.89
Full framework (+LIC)	0.947	0.85	0.94	0.947

Table 7. Comparative analysis of the proposed model with SOTA architectures.

Methods	Oil Spill Class	mIoU	Precision	Recall	F1-Score
U-Net	80.13	86.33	87.65	90.34	88.97
E-Net	70.23	79.52	83.64	81.42	82.51
DeepLabV3	84.71	89.58	91.63	91.82	91.72
Ours	85.0	94.7	≈94.0 (at 0.294)	94.0	94.0

Table 8. Evaluation of the proposed method model relative to existing research in oil spill detection.

Method	Data Type	mIoU (%)	F1-Score	Precision
U-Net	Optical	86.33	88.97	87.65
E-Net	Optical	79.52	82.51	83.64
DeepLabV3	Optical	89.58	91.72	91.63
[41]	Optical	-	0.72	0.77
[28]	SAR	88.4	-	-
[34]	SAR	-	-	-
[36]	SAR	91.2	-	-
Proposed (ours)	Optical	0.947	0.94	0.94

7. Conclusions

This study presents a robust oil spill detection framework that addresses the limitations of existing datasets and conventional monitoring approaches. Recognizing that model performance heavily depends on dataset diversity and quality, we developed a custom oil spill dataset through advanced blending-based augmentation techniques. By integrating oil spill regions into various oceanic backgrounds under diverse environmental conditions, the dataset improves model generalization across realistic maritime scenarios. Additionally, the incorporation of the LIC method enhances the representation of ocean wave dynamics, enabling more realistic segmentation mask generation and improving detection sensitivity in complex water surfaces. Fine-tuning the YOLOv11m-seg model on the proposed dataset resulted in superior performance compared to established segmentation architectures. Quantitative evaluation demonstrates that the proposed framework achieves the highest mIoU (94.7%), precision, recall, and F1-scores. These findings validate the effectiveness of combining synthetic data augmentation, environmental variability modeling, and SOTA deep learning architecture for oil spill detection.

Author Contributions: Conceptualization, F.A.; Methodology, F.A.; Software, F.B.; Validation, F.B.; Formal analysis, K.T.A.; Data curation, K.T.A.; Writing—review & editing, F.M. All authors have read and agreed to the published version of the manuscript.

Funding: This research is not receiving external funding.

Data Availability Statement: Dataset is available by request.

Acknowledgments: We thank all authors for their support in doing this research work.

Conflicts of Interest: The authors declare no conflicts of interest.

References

1. Jiao, Z.; Jia, G.; Cai, Y. A New Approach to Oil Spill Detection That Combines Deep Learning with Unmanned Aerial Vehicles. *Comput. Ind. Eng.* **2019**, *135*, 1300–1311. [CrossRef]
2. Available online: https://www.itopf.org/knowledge-resources/data-statistics/statistics/ (accessed on 23 October 2025).
3. Available online: https://www.noaa.gov/education/resource-collections/ocean-coasts/oil-spills (accessed on 5 November 2025).
4. Yekeen, S.T.; Balogun, A.-L.; Yusof, K.B.W. A novel deep learning instance segmentation model for automated marine oil spill detection. *ISPRS J. Photogramm. Remote Sens.* **2020**, *167*, 190–200.
5. Grau, M.V.; Groves, T. The oil spill process: The effect of coast guard monitoring on oil spills. *Environ. Resour. Econ.* **1997**, *10*, 315–339. [CrossRef]
6. Senga, H.; Kato, N.; Ito, A.; Niou, H.; Yoshie, M.; Fujita, I.; Igarashi, K.; Okuyama, E. Spilled oil tracking autonomous buoy system. *Adv. Robot.* **2009**, *23*, 1103–1129. [CrossRef]
7. Griffo, G.; Piper, L.; Lay-Ekuakille, A.; Pellicanò, D. Design of buoy station for marine pollutant detection. *Measurement* **2014**, *47*, 1024–1029.
8. Akhmedov, F.; Khujamatov, H.; Abdullaev, M.; Jeon, H.-S. A Novel Oil Spill Dataset Augmentation Framework Using Object Extraction and Image Blending Techniques. *Remote Sens.* **2025**, *17*, 336. [CrossRef]
9. Akhmedov, F.; Nasimov, R.; Abdusalomov, A. Developing a Comprehensive Oil Spill Detection Model for Marine Environments. *Remote Sens.* **2024**, *16*, 3080. [CrossRef]
10. Cao, Y.; Xu, L.; Clausi, D. Exploring the potential of active learning for automatic identification of marine oil spills using 10-year (2004–2013) RADARSAT data. *Remote Sens.* **2017**, *9*, 41. [CrossRef]
11. Xu, L.; Li, J.; Brenning, A. A comparative study of different classification techniques for marine oil spill identification using RADARSAT-1 imagery. *Remote Sens. Environ.* **2014**, *141*, 14–23. [CrossRef]
12. Kim, T.S.; Park, K.A.; Li, X.; Lee, M.; Hong, S.; Lyu, S.J.; Nam, S. Detection of the hebei spirit oil spill on SAR imagery and its temporal evolution in a coastal region of the Yellow sea. *Adv. Space Res.* **2015**, *56*, 1079–1093. [CrossRef]
13. Ozkan, C.; Osmanoglu, B.; Sunar, F.; Staples, G.; Kalkan, K.; Balık Sanlı, F. Testing the generalization efficiency of oil slick classification algorithm using multiple Sar data for deepwater horizon oil spill. *ISPRS Int. Arch. Photogramm. Remote Sens. Spat. Inf. Sci.* **2012**, *XXXIX-B7*, 67–72. [CrossRef]
14. Skrunes, S.; Brekke, C.; Eltoft, T. Characterization of marine surface slicks by radarsat-2 multipolarization features. *IEEE Trans. Geosci. Remote Sens.* **2014**, *52*, 5302–5319. [CrossRef]
15. Marghany, M. Automatic Mexico gulf oil spill detection from Radarsat-2 SAR satellite data using genetic algorithm. *Acta Geophys.* **2016**, *64*, 1916–1941. [CrossRef]
16. Marghany, M. Automatic Detection of oil spill disasters along gulf of Mexico using RADARSAT-2 SAR data. *J. Indian Soc. Remote Sens.* **2017**, *45*, 503–511. [CrossRef]
17. Song, D.; Ding, Y.; Li, X.; Zhang, B.; Xu, M. Ocean oil spill classification with RADARSAT-2 SAR based on an optimized wavelet neural network. *Remote Sens.* **2017**, *9*, 799. [CrossRef]
18. Joseph, M.; Jayasri, P.V.; Dutta, S.; Kumari, E.V.S.S.; Prasad, A.V.V. Oil spill detection from RISAT-1 imagery using texture analysis. In Proceedings of the 2016 Asia-Pacific Microwave Conference (APMC), New Delhi, India, 5–9 December 2016.
19. Chaudhary, V.; Kumar, S. Marine oil slicks detection using spaceborne and airborne SAR data. *Adv. Space Res.* **2020**, *66*, 854–872. [CrossRef]
20. Lin, Y.; Yu, J.; Zhang, Y.; Wang, P.; Ye, Z. Dynamic analysis of oil spill in Yangtze estuary with HJ-1 imagery. In *Geo-Informatics in Resource Management and Sustainable Ecosystem*; Communications in Computer and Information Science; Springer: Berlin/Heidelberg, Germany, 2016; Voume 569, pp. 345–356.
21. De Carolis, G.; Adamo, M.; Pasquariello, G. Thickness estimation of marine oil slicks with near-infrared MERIS and MODIS imagery: The Lebanon oil spill case study. In Proceedings of the International Geoscience and Remote Sensing Symposium, Munich, Germany, 22–27 July 2012; pp. 3002–3005.
22. Adamo, M.; de Carolis, G.; de Pasquale, V.; Pasquariello, G. Detection and tracking of oil slicks on sun-glittered visible and near infrared satellite imagery. *Int. J. Remote Sens.* **2009**, *30*, 6403–6427. [CrossRef]
23. Pérez-García, Á.; Rodríguez-Molina, A.; Hernández, E.; López, J.F. Spectral indices survey for oil spill detection in coastal areas. *IEEE J. Sel. Top. Appl. Earth Obs. Remote Sens.* **2024**, *17*, 15359–15372. [CrossRef]
24. Dubucq, D.; Sicot, G.; Lennon, M.; Miegebielle, V. Detection and discrimination of the thick oil patches on the sea surface. *Int. Arch. Photogramm. Remote Sens. Spatial Inf. Sci.* **2016**, *XLI-B8*, 417–421. [CrossRef]
25. Pisano, A.; Bignami, F.; Santoleri, R. Oil spill detection in glint-contaminated near-infrared MODIS imagery. *Remote Sens.* **2015**, *7*, 1112–1134. [CrossRef]
26. Mera, D.; Bolon-Canedo, V.; Cotos, J.M.; Alonso-Betanzos, A. On the use of feature selection to improve the detection of sea oil spills in SAR images. *Comput. Geosci.* **2017**, *100*, 166–178. [CrossRef]

27. Terrance, V.; Graham, W.T. Dataset augmentation in feature space. In Proceedings of the International Conference on Machine Learning (ICML), Workshop Track, Sydney, Australia, 6–11 August 2017.
28. Li, Y.; Cui, C.; Liu, Z.; Liu, B.; Xu, J.; Zhu, X.; Hou, Y. Detection and monitoring of oil spills using moderate/high-resolution remote sensing images. *Arch. Environ. Contam. Toxicol.* **2017**, *73*, 154–169.
29. Tian, W.; Bian, X.; Shao, Y.; Zhang, Z. On the detection of oil spill with China's HJ-1C SAR image. *Aquat. Procedia* **2015**, *3*, 144–150.
30. Tong, S.; Liu, X.; Chen, Q.; Zhang, Z.; Xie, G. Multi-feature based ocean oil spill detection for polarimetric SAR data using random forest and the self-similarity parameter. *Remote Sens.* **2019**, *11*, 451. [CrossRef]
31. El-Magd, I.A.; Zakzouk, M.; Abdulaziz, A.M.; Ali, E.M. The potentiality of operational mapping of oil pollution in the mediterranean sea near the entrance of the suez canal using sentinel-1 SAR data. *Remote Sens.* **2020**, *12*, 1352. [CrossRef]
32. Bayramov, E.; Kada, M.; Buchroithner, M. Monitoring oil spill hotspots, contamination probability modelling and assessment of coastal impacts in the Caspian Sea using SENTINEL-1, LANDSAT-8, RADARSAT, ENVISAT and ERS satellite sensors. *J. Oper. Oceanogr.* **2018**, *11*, 27–43. [CrossRef]
33. Yu, Q.; Clausi, D.A. IRGS: Image segmentation using edge penalties and region growing. *IEEE Trans. Pattern Anal. Mach. Intell.* **2008**, *30*, 2126–2139. [CrossRef]
34. Zhang, B.; Perrie, W.; Li, X.; Pichel, W.G. Mapping sea surface oil slicks using RADARSAT-2 quad-polarization SAR image. *Geophys. Res. Lett.* **2011**, *38*, 415–421. [CrossRef]
35. Del Frate, F.; Petrocchi, A.; Lichtenegger, J.; Calabresi, G. Neural networks for oil spill detection using ERS-SAR data. *IEEE Trans. Geosci. Remote Sens.* **2000**, *38*, 2282–2287. [CrossRef]
36. Chen, S.; Wang, H.; Xu, F.; Jin, Y.-Q. Target classification using the deep convolutional networks for SAR images. *IEEE Trans. Geosci. Remote Sens.* **2016**, *54*, 4806–4817. [CrossRef]
37. Xu, Q.; Li, X.; Wei, Y.; Tang, Z.; Cheng, Y.; Pichel, W.G. Satellite observations and modeling of oil spill trajectories in the Bohai sea. *Mar. Pollut. Bull.* **2013**, *71*, 107–116. [CrossRef]
38. Hasan, M.; Ullah, S.; Khan, M.J.; Khurshid, K. Comparative analysis of SVM, ANN and CNN for classifying vegetation species using hyperspectral thermal infrared data. *Int. Arch. Photogramm. Remote Sens. Spat. Inf. Sci.* **2019**, *42*, 1861–1868. [CrossRef]
39. Topouzelis, K.; Singha, S. *Oil Spill Detection Using Space-Borne Sentinel-1 SAR Imagery*; Elsevier: Amsterdam, The Netherlands, 2017.
40. Loos, E.; Brown, L.; Borstad, G.; Mudge, T.; Alvarez, M. Characterization of oil slicks at sea using remote sensing techniques. In Proceedings of the IEEE Oceans, Hampton Roads, VA, USA, 14–19 October 2012; pp. 1–4.
41. De Kerf, T.; Sels, S.; Samsonova, S.; Vanlanduit, S. Oil spill drone: A dataset of drone-captured, segmented RGB images for oil spill detection in port environments. *arXiv* **2024**, arXiv:2402.18202. [CrossRef]
42. Jiang, Z.; Zhang, J.; Ma, Y.; Mao, X.; Du, K. Research on dual-driven identification of oil-spill type based on optical and thermal characteristics. *IEEE Trans. Geosci. Remote Sens.* **2024**, *62*, 4209618. [CrossRef]
43. Jiang, Z.; Zhang, J.; Ma, Y.; Mao, X.; Du, K.; Huang, X. Research on cross-spatiotemporal remote sensing detection of marine oil spills and emulsions based on coupling optical and thermal response characteristics. *IEEE Trans. Geosci. Remote Sens.* **2024**, *62*, 4209721. [CrossRef]
44. Jiang, Z.; Zhang, J.; Ma, Y.; Mao, X. Research on remote sensing quantitative inversion of oil spills and emulsions using fusion of optical and thermal characteristics. *IEEE J. Sel. Top. Appl. Earth Obs. Remote Sens.* **2025**, *18*, 8472–8489. [CrossRef]

Disclaimer/Publisher's Note: The statements, opinions and data contained in all publications are solely those of the individual author(s) and contributor(s) and not of MDPI and/or the editor(s). MDPI and/or the editor(s) disclaim responsibility for any injury to people or property resulting from any ideas, methods, instructions or products referred to in the content.